



This is a repository copy of *Weak imposition of Dirichlet boundary conditions for analyses using Powell–Sabin B-splines*.

White Rose Research Online URL for this paper:

<https://eprints.whiterose.ac.uk/181918/>

Version: Accepted Version

Article:

Chen, L. and de Borst, R. (2021) Weak imposition of Dirichlet boundary conditions for analyses using Powell–Sabin B-splines. *International Journal for Numerical Methods in Engineering*, 122 (23). pp. 6888-6904. ISSN 0029-5981

<https://doi.org/10.1002/nme.6815>

This is the peer reviewed version of the following article: Chen, L, Borst, R. Weak imposition of Dirichlet boundary conditions for analyses using Powell–Sabin B-splines. *Int J Numer Methods Eng.* 2021; 122(23): 6888– 6904., which has been published in final form at <https://doi.org/10.1002/nme.6815>. This article may be used for non-commercial purposes in accordance with Wiley Terms and Conditions for Use of Self-Archived Versions. This article may not be enhanced, enriched or otherwise transformed into a derivative work, without express permission from Wiley or by statutory rights under applicable legislation. Copyright notices must not be removed, obscured or modified. The article must be linked to Wiley’s version of record on Wiley Online Library and any embedding, framing or otherwise making available the article or pages thereof by third parties from platforms, services and websites other than Wiley Online Library must be prohibited.

Reuse

Items deposited in White Rose Research Online are protected by copyright, with all rights reserved unless indicated otherwise. They may be downloaded and/or printed for private study, or other acts as permitted by national copyright laws. The publisher or other rights holders may allow further reproduction and re-use of the full text version. This is indicated by the licence information on the White Rose Research Online record for the item.

Takedown

If you consider content in White Rose Research Online to be in breach of UK law, please notify us by emailing eprints@whiterose.ac.uk including the URL of the record and the reason for the withdrawal request.



eprints@whiterose.ac.uk
<https://eprints.whiterose.ac.uk/>

Weak imposition of Dirichlet boundary conditions for analyses using Powell-Sabin B-splines

Lin Chen, René de Borst*

University of Sheffield, Department of Civil and Structural Engineering, Sheffield S1 3JD, UK

SUMMARY

Powell-Sabin B-splines are enjoying an increased use in the analysis of solids and fluids, including fracture propagation. However, the Powell-Sabin B-spline interpolation does not hold the Kronecker delta property and, therefore, the imposition of Dirichlet boundary conditions is not as straightforward as for the standard finite elements. Herein we discuss the applicability of various approaches developed to date for the weak imposition of Dirichlet boundary conditions in analyses which employ Powell-Sabin B-splines. We take elasticity and fracture propagation using phase-field modelling as a benchmark problem. We first succinctly recapitulate the phase-field model for propagation of brittle fracture, which encapsulates linear elasticity, and its discretisation using Powell-Sabin B-splines. As baseline solution we impose Dirichlet boundary conditions in a strong sense, and use this to benchmark the Lagrange multiplier, penalty and Nitsches methods, as well as methods based on the Hellinger – Reissner principle, and the linked Lagrange multiplier method and its modified version. Copyright © 2018 John Wiley & Sons, Ltd.

Received . . .

KEY WORDS: Dirichlet boundary conditions; Powell-Sabin B-splines; weak imposition; fracture.

1. INTRODUCTION

Powell-Sabin B-splines are bivariate splines defined on unstructured triangulations [1] yielding C^1 continuity. Compared with tensor product B-splines, Powell-Sabin B-splines allow for a straightforward adaptive refinement of the mesh. Indeed, remeshing is standard since established algorithms for remeshing of triangles in the physical domain can be exploited. For this reason, they can be used straightforwardly in two-dimensional analyses of solids and fluids. For instance, Speleers et al. [2] have employed Powell-Sabin B-splines to solve advection-diffusion-reaction problems, while Giorgiani and co-workers [3] have developed a Powell-Sabin scheme for the solution of the 2D Euler equations in the supersonic regime. May et al. have utilised Powell-Sabin B-splines to analyse bending of Kirchhoff-Love plates and damage evolution [4, 5]. Also Chen and de Borst used for the propagation and damage evolution problems [6–9].

A disadvantage of Powell-Sabin B-splines is that they do not hold the Kronecker delta property. Thus, the imposition of Dirichlet boundary conditions is not as straightforward as in finite element methods. Speleers et al. [10, 11] treated Dirichlet boundary conditions imposed on Powell-Sabin B-splines in the context of a finite element framework. Speleers et al. employed [2] Hermite basis functions instead of B-spline basis functions to define the Powell-Sabin splines. However, the Hermite basis does not form a partition of unity. Da Veiga et al. [12] used the Powell-Sabin B-splines to address the Reissner-Mindlin plate problem, in which the Dirichlet boundary conditions

*Correspondence to: R. de Borst, University of Sheffield, Department of Civil and Structural Engineering, Sheffield S1 3JD, UK. E-mail: r.deborst@sheffield.ac.uk

are imposed in a combination of strong format and weak form (Nitsche type). Giorgiani et al. [3] used a strong format to impose Dirichlet boundary conditions, which is possible when an analytical solution is available for the problem. May et al. [5] and Chen et al. [6] used a linear interpolation function to approximate the boundary values of Powell-Sabin B-splines. However, a systematic study of the imposition of Dirichlet boundary condition when using Powell-Sabin B-splines is not available.

In recent years many techniques have been developed for the implementation of Dirichlet boundary conditions in numerical techniques which are non-interpolatory such mesh-free methods. These techniques modify the weak form of the problem at hand by adding terms to the energy functional. Examples are the Lagrange multiplier and penalty methods, Nitsche's trick, the Hellinger - Reissner (H-R) principle, and the linked Lagrange multiplier (LLM) method and its modified version [13]. The aim of this contribution is to compare these techniques for the imposition of Dirichlet boundary conditions when using Powell-Sabin B-splines. Furthermore, we link the parametric behaviour of some methods with convergence theories, which provides guidance on the choice of the algorithmic parameters.

Fracture propagation is taken as a benchmark problem to illustrate the concept of imposing Dirichlet boundary conditions. For this reason we present a concise summary of phase-field approximations of brittle fracture in anisotropic materials, followed by a review of the construction of Powell-Sabin B-splines. Subsequently, we review and compare the aforementioned techniques based on a modification of the weak form to impose Dirichlet boundary conditions. Two case studies subsequently illustrate the numerical performance of these approaches: convergence aspects, and the capturing of a characteristic physical phenomenon like crack kinking and zigzag crack propagation.

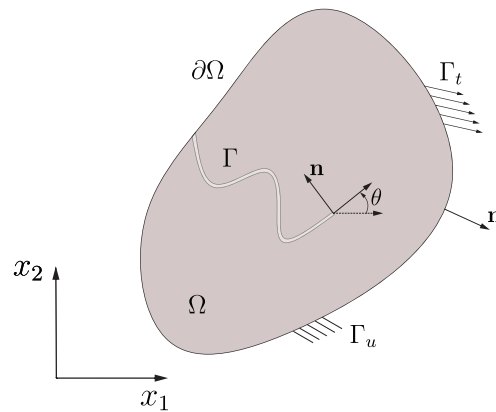


Figure 1. Two-dimensional crack (Γ) with a unit vector \mathbf{n} normal to the crack path and the boundary.

2. PROBLEM STATEMENT

Figure 1 illustrates a cracked domain Ω , bounded by Γ_b such that, $\Gamma_b = \Gamma_t \cup \Gamma_u$. Γ_u is the Dirichlet boundary with prescribed displacements $\hat{\mathbf{u}}$. Γ_t denotes the Neumann boundary with prescribed tractions. Γ is the set of cracks where displacement fields $\mathbf{u} \in \mathcal{H}^1(\Omega \setminus \Gamma)$ can jump. \mathcal{H}^1 denotes the Sobolev space of functions with square integrable first derivatives. \mathbf{n} is the unit vector normal to the surfaces.

A quasi-static crack propagation problem is considered as a representative example. A phase-field model is used herein for modelling the fracture propagation. The phase-field approach to brittle fracture has its origins in the so-called variational approach to fracture [14]. In it, crack initiation and propagation are considered as a minimisation problem of a Griffith-like energy functional. The

total energy functional for the cracked body then reads:

$$\begin{aligned}\mathcal{E}(\mathbf{u}, \Gamma) &= \mathcal{E}_u(\mathbf{u}, \Gamma) - W_{\text{ext}} + \mathcal{E}_s(\Gamma) \\ &= \int_{\Omega \setminus \Gamma} \mathcal{W}(\mathbf{u}) \, d\Omega - \int_{\Gamma_t} \mathbf{u} \cdot \hat{\mathbf{t}} \, d\Gamma + \int_{\Gamma} G_c(\mathbf{n}) \, d\Gamma,\end{aligned}\quad (1)$$

where the first term denotes the elastic energy, with $\mathcal{W}(\mathbf{u})$ being the energy density function. In this contribution, isotropic linear elasticity is used such that $\mathcal{W}(\mathbf{u}) = \mu \boldsymbol{\varepsilon}(\mathbf{u}) \cdot \boldsymbol{\varepsilon}(\mathbf{u}) + \lambda/2 \text{tr}(\boldsymbol{\varepsilon}(\mathbf{u}))^2$ with $\boldsymbol{\varepsilon}$ the small-strain tensor, and λ and μ Lamé's constants. The second term is the potential energy of external forces. The last term represents the anisotropic surface energy required to create the crack according to the Griffith criterion. $G_c(\mathbf{n})$ is an orientation-dependent fracture toughness.

Due to unknown locations of the displacement jump in the Griffith's energy functional we must reformulate Equation (1) in a regularised form: cracks are represented by a scalar phase field variable d , ranging from 0 (away from the crack) to 1 (completely broken state):

$$\begin{aligned}\mathcal{E}(\mathbf{u}, d) &= \mathcal{E}_u(\mathbf{u}, d) - W_{\text{ext}} + \mathcal{E}_s(d) \\ &= \int_{\Omega} \mathcal{W}(\mathbf{u}, d) \, d\Omega - \int_{\Gamma_t} \mathbf{u} \cdot \hat{\mathbf{t}} \, d\Gamma + G_0 \int_{\Omega} \gamma(d) \, d\Omega,\end{aligned}\quad (2)$$

where G_0 is a scaling factor with the dimension of energy per unit surface, $\gamma(d)$ being the crack density function per unit volume. Obviously, in the absence of damage ($d = 0$), Equation (2) becomes the classical linear-elastic energy functional.

A staggered approach is adopted for the solution of the coupled non-linear problem in Equation (2) [15]. In the time-discrete evolution, given the displacement field $\mathbf{u}^{(i-1)}$ and the phase field $d^{(i-1)}$ at time t_{i-1} , the solution at time t_i is obtained by solving the stationarity conditions for the functional, Equation (2), under the unilateral constraint $d_n \geq d^{(i-1)}$, n being the iteration number. The problem is hence split into a 'displacement' sub-problem and a 'damage' sub-problem. At each time, the two sub-problems are solved iteratively until a convergence criterion is met.

The 'displacement' sub-problem consists of the minimisation for \mathbf{u}_h when the phase-field variable d_h has been fixed:

$$\mathbf{u} = \text{Arg} \min_{\mathbf{u} \in \mathcal{S}_u} \{ \mathcal{E}_u(\mathbf{u}, d) - W_{\text{ext}} \}, \quad (3)$$

where $\mathcal{S}_u = \{ \mathbf{u} \in \mathcal{H}^1(\Omega), \mathbf{u}|_{\Gamma_u} = \hat{\mathbf{u}} \}$ and $\hat{\mathbf{u}}$ represents the prescribed displacements at Γ_u . For the 'damage' sub-problem, the solution for d_h is obtained through the minimisation of Equation (2) at a fixed \mathbf{u}_h :

$$d = \text{Arg} \min_{d \in \mathcal{S}_d} \{ \mathcal{E}_u(\mathbf{u}, d) + \mathcal{E}_s(d) \}, \quad (4)$$

where $\mathcal{S}_d = \{ d \in \mathcal{H}^1(\Omega), d|_{\Gamma_d} = \hat{d} \}$ and \hat{d} denotes the phase-field at Γ_d . For conciseness we herein do not consider phase-field boundaries Γ_d .

In the present study Powell-Sabin B-splines have been used to discretise the solution space. They describe the geometry and interpolate the displacement field \mathbf{u} and the phase field d in an isoparametric sense:

$$\mathbf{x} = \sum_{k=1}^{N_v} \sum_{j=1}^3 N_k^j \mathbf{X}_k^j = \mathbf{N}^e \mathbf{X}^e \quad \mathbf{u} = \sum_{k=1}^{N_v} \sum_{j=1}^3 N_k^j \mathbf{U}_k^j = \mathbf{N}^e \mathbf{U}^e \quad d = \sum_{k=1}^{N_v} \sum_{j=1}^3 N_k^j d_k^j = \mathbf{N}^e \mathbf{d}^e, \quad (5)$$

where \mathbf{X}_k^j represent the coordinates of the corners \mathbf{Q}_k^j of Powell-Sabin triangles, Figure 2. \mathbf{U}_k^j and α_k^j denote the degrees of freedom at \mathbf{Q}_k^j and N_v is the total number of vertices. The indices $j = 1, 2, 3$ imply that three Powell-Sabin B-splines are defined on each vertex k . \mathbf{N}^e , \mathbf{X}^e , \mathbf{U}^e and \mathbf{d}^e are shape functions, coordinates, and degrees of freedom associated with each element e .

We now give a succinct description of Powell-Sabin B-splines [16]. We consider a triangulation \mathcal{T} with \mathcal{L} triangles and N_v vertices, denoted by thick black lines in Figure 2(a). The triangulation \mathcal{T} can

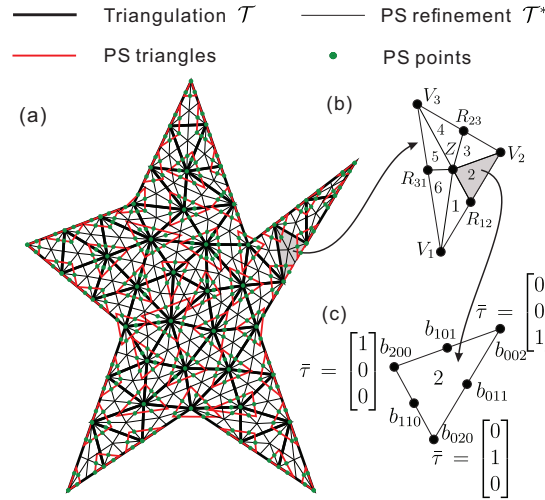


Figure 2. Example of a triangulation \mathcal{T} (thick black lines), Powell-Sabin refinement \mathcal{T}^* (thin black lines) of \mathcal{T} , Powell-Sabin triangles (red) and Powell-Sabin points (blue). In (b) each triangle e is subdivided into six mini-triangles. In (c) each mini-triangle has a barycentric coordinate system $\bar{\tau}$.

be generated by any package for standard triangular elements, such as Gmsh [17]. To derive Powell-Sabin B-splines, each triangle e is divided into six ($n = 1, 2, \dots, 6$) mini-triangles, cf. Figure 2(b). This yields the Powell-Sabin refinement \mathcal{T}^* . For each vertex k of the triangulation \mathcal{T} , we can obtain the Powell-Sabin points (shown in green in Figure 2(a)) by the vertex itself and points lying at the centre of the edges of \mathcal{T}^* . To obtain positive basis functions, we introduce a Powell-Sabin triangle (shown in red in Figure 2(a)) to comprise all the Powell-Sabin points. Herein, we employ the algorithm of [18] to find the minimum area triangle which encloses the convex polygon defined by Powell-Sabin points. We further constrain Powell-Sabin triangles on the boundary as follows: (1) for an angle of $\gamma < 180^\circ$ two edges of the Powell-Sabin triangle lie on the boundary; (2) for an angle of $\gamma = 180^\circ$ one edge of the Powell-Sabin triangle lies on the boundary, cf. Figure 3.

After obtaining the Powell-Sabin triangle for each vertex k , the basis functions can be computed. Three Powell-Sabin B-splines N_k^j , $j = 1, 2, 3$, are defined on each vertex k with coordinates $\mathbf{V}_k = (x_1^k, x_2^k)$. Powell-Sabin B-splines have the following properties. For any $\mathbf{V}_k \neq \mathbf{V}_l$ we have:

$$N_k^j(\mathbf{V}_l) = 0, \quad \frac{\partial}{\partial x_1} N_k^j(\mathbf{V}_l) = 0, \quad \frac{\partial}{\partial x_2} N_k^j(\mathbf{V}_l) = 0, \quad (6)$$

and otherwise

$$N_k^j(\mathbf{V}_k) = \eta_k^j, \quad \frac{\partial}{\partial x_1} N_k^j(\mathbf{V}_k) = \beta_k^j, \quad \frac{\partial}{\partial x_2} N_k^j(\mathbf{V}_k) = \gamma_k^j, \quad (7)$$

with

$$\sum_{j=1}^3 \eta_k^j = 1, \quad \sum_{j=1}^3 \beta_k^j = 0, \quad \sum_{j=1}^3 \gamma_k^j = 0. \quad (8)$$

The coefficients η_k^j , β_k^j and γ_k^j are obtained for each vertex k by solving:

$$\begin{bmatrix} \eta_k^1 & \eta_k^2 & \eta_k^3 \\ \beta_k^1 & \beta_k^2 & \beta_k^3 \\ \gamma_k^1 & \gamma_k^2 & \gamma_k^3 \end{bmatrix} \begin{bmatrix} x^{k,1} & y^{k,1} & 1 \\ x^{k,2} & y^{k,2} & 1 \\ x^{k,3} & y^{k,3} & 1 \end{bmatrix} = \begin{bmatrix} x^k & y^k & 1 \\ 1 & 0 & 0 \\ 0 & 1 & 0 \end{bmatrix}, \quad (9)$$

where $\mathbf{Q}_k^j = (x^{k,j}, y^{k,j})$ are the coordinates of the Powell-Sabin triangle corners associated with vertex k . When the coefficients η_k^j , β_k^j and γ_k^j have been determined we can compute the Bézier

extraction operator C^e for element e . This allows for an efficient computation of basis functions and their derivatives as a traditional finite-element data structure can be employed. For instance, the basis functions N^e in Equation (5) are computed from:

$$N^e = C^e B, \quad (10)$$

with the six Bernstein polynomials, contained in the vector B [6].

Normally, the shape function inside a triangular element is associated with 3×3 Powell-Sabin triangle corners or degrees of freedom. Here, the first '3' represents the three Powell-Sabin triangle corners of each vertex, while the second '3' links to the three vertices of each triangle element. The dimension of the vector N^e and the matrix C^e are 9×1 and 9×6 , respectively. Each row of N^e and C^e denotes the contribution of the Powell-Sabin triangle corner related to the element vertex.

A special case arises when computing the shape function along the triangle element boundary, e.g., on the side V_1V_2 in Figure 2(b). The boundary shape function is then only related to the two vertices at the element boundary itself, for instance vertex V_1 and V_2 on side V_1V_2 , which yields 3×2 degrees of freedom. Then, Equations (5) and (10) reduce to:

$$[N_b^e]_{6 \times 1} = [C_b^e]_{6 \times 6} [B]_{6 \times 1}, \quad \mathbf{x}_b = N_b^e \mathbf{X}_b^e, \quad (11)$$

with N_b^e the boundary shape function vector, C_b^e the Bézier extraction operator which comprises the coefficients of the Powell-Sabin triangle corners linked to the element boundary vertices only, and \mathbf{x}_b and \mathbf{X}_b^e denote the coordinates at the element boundary and the coordinates of Powell-Sabin triangle corners linked to the element boundary vertices, respectively.

3. IMPOSING DIRICHLET BOUNDARY CONDITIONS

Equations (7) and (8) show that Powell-Sabin B-splines do not hold the Kronecker-delta property and are non-interpolatory at the vertex. Thus, imposing $\mathbf{u} = \hat{\mathbf{u}}$ on Γ_u is not as trivial as in standard finite elements, and the weak form defined by Equation (2) cannot be employed. In this section, we will discuss methods for imposing Dirichlet boundary conditions which circumvent this issue. For conciseness we only consider displacement-type Dirichlet boundary conditions. Correspondingly, the 'damage' sub-problem in Equation (4) remains unchanged. Only the 'displacement' sub-problem (3) must be modified to enforce the displacement boundary conditions.

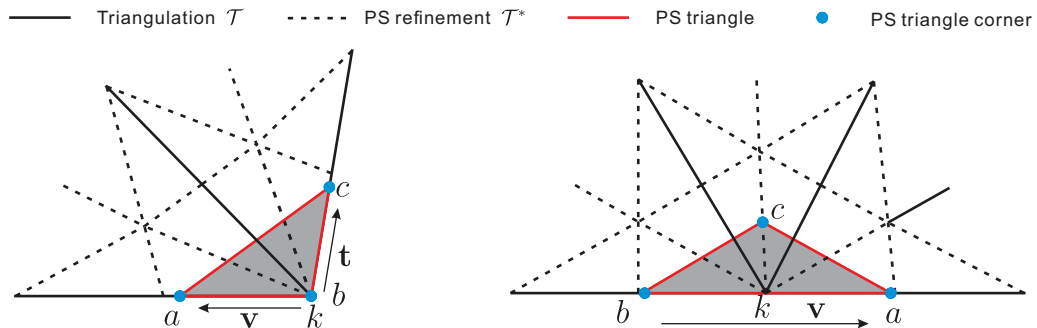


Figure 3. Imposing Dirichlet boundary conditions strongly at the corners of a Powell-Sabin triangle on boundary vertices with an angle different from π (left) and equal to π (right).

3.1. Imposing Dirichlet boundary conditions strongly

When an analytical solution is available one can impose Dirichlet boundary conditions strongly [10]. This is done as follows. In Section 2 a special choice of the Powell-Sabin triangle is given along the boundary: (i) for vertex k with an angle $\gamma < 180^\circ$, with two sides of the Powell-Sabin triangle placed

along two boundary edges, see Figure 3(left); (ii) for vertex k with an angle $\gamma = 180^\circ$ one side of the Powell-Sabin triangle lies at the boundary edge, see Figure 3(right). Reformulating Equation (9) in terms of the nodal degrees of freedom U results in:

$$\begin{bmatrix} \eta_k^a & \eta_k^b & \eta_k^c \\ \beta_k^a & \beta_k^b & \beta_k^c \\ \gamma_k^a & \gamma_k^b & \gamma_k^c \end{bmatrix} \begin{bmatrix} U^{k,a} \\ U^{k,b} \\ U^{k,c} \end{bmatrix} = \begin{bmatrix} U^k \\ \frac{\partial U^k}{\partial x_1} \\ \frac{\partial U^k}{\partial x_2} \end{bmatrix}, \quad (12)$$

where $U^{k,i}$ is the nodal degree of freedom of the Powell-Sabin triangle corner i ($i = a, b, c$), associated with vertex k , U^k denoting the displacement at vertex k . $\nabla U^k = \left[\frac{\partial U^k}{\partial x_1} \quad \frac{\partial U^k}{\partial x_2} \right]$ is the gradient of U^k .

For the case $\gamma < 180^\circ$, the coefficients η_k^i , β_k^i and γ_k^i ($i = a, b, c$) satisfy:

$$\begin{aligned} \eta_k^a &= \eta_k^c = 0, & \eta_k^b &= 1, \\ \begin{bmatrix} \beta_k^a \\ \gamma_k^a \end{bmatrix} \cdot \mathbf{t} &= 0, & \begin{bmatrix} \beta_k^c \\ \gamma_k^c \end{bmatrix} \cdot \mathbf{v} &= 0, \end{aligned} \quad (13)$$

with \mathbf{t} and \mathbf{v} being unit vectors along the boundary, see Figure 3(left)

$$\mathbf{t} = \frac{\mathbf{x}_a - \mathbf{x}_b}{\|\mathbf{x}_a - \mathbf{x}_b\|}, \quad \mathbf{v} = \frac{\mathbf{x}_c - \mathbf{x}_b}{\|\mathbf{x}_c - \mathbf{x}_b\|} \quad (14)$$

From Equations (12) and (13), we have:

$$U^{k,b} = U^k, \quad U^{k,a} = U^k + \frac{\nabla U^k \cdot \mathbf{v}}{\begin{bmatrix} \beta_k^a \\ \gamma_k^a \end{bmatrix} \cdot \mathbf{v}}, \quad U^{k,c} = U^k + \frac{\nabla U^k \cdot \mathbf{t}}{\begin{bmatrix} \beta_k^c \\ \gamma_k^c \end{bmatrix} \cdot \mathbf{t}} \quad (15)$$

For the case $\gamma = 180^\circ$ the coefficients η_k^i , β_k^i and γ_k^i ($i = a, b, c$) guarantee

$$\begin{aligned} \eta_k^a &\neq 0, & \eta_k^b &\neq 0, & \eta_k^c &= 0, \\ \begin{bmatrix} \beta_k^c \\ \gamma_k^c \end{bmatrix} \cdot \mathbf{v} &= 0, \end{aligned} \quad (16)$$

where \mathbf{v} denotes the unit vector along the boundary given in Equation (14), see Figure 3(right). Equations (12) and (16) lead to:

$$U^{k,a} = \frac{U^k \Delta_1 - \eta_k^b \nabla U^k \cdot \mathbf{v}}{\eta_k^a \Delta_1 - \eta_k^b \Delta}, \quad U^{k,b} = \frac{-U^k \Delta + \eta_k^a \nabla U^k \cdot \mathbf{v}}{\eta_k^a \Delta_1 - \eta_k^b \Delta}, \quad (17)$$

with $\Delta = \begin{bmatrix} \beta_k^a \\ \gamma_k^a \end{bmatrix} \cdot \mathbf{v}$, $\Delta_1 = \begin{bmatrix} \beta_k^b \\ \gamma_k^b \end{bmatrix} \cdot \mathbf{v}$.

Remark 1: Once $U^{k,i}$ has been obtained, we can apply it directly in the system of equations like in standard finite elements. We consider this way of imposing Dirichlet boundary conditions be a strong format comparing to following approaches which employ a weak imposition of the boundary conditions. The displacement $U^{k,i}$ at each Powell-Sabin triangle corner is derived analytically in Equations (15) and (17). We refer to this solution as the *optimal solution*.

3.2. Lagrange multiplier method

Dirichlet boundary conditions can be enforced weakly by introducing Lagrange multipliers λ to the energy functional related to the displacement sub-problem (3), as follows:

$$\begin{aligned} \mathcal{E}_L(\mathbf{u}, d, \lambda) &= \mathcal{E}_u(\mathbf{u}, d) - W_{\text{ext}} + \mathcal{E}_l(\mathbf{u}, \lambda) \\ &= \int_{\Omega} \mathcal{W}(\mathbf{u}, d) \, d\Omega - \int_{\Gamma_t} \mathbf{u} \cdot \hat{\mathbf{t}} \, d\Gamma + \int_{\Gamma_u} \lambda \cdot (\mathbf{u} - \hat{\mathbf{u}}) \, d\Gamma, \end{aligned} \quad (18)$$

so that the 'displacement' sub-problem (3) is reformulated as:

$$(\mathbf{u}, \boldsymbol{\lambda}) = \text{Arg} \min_{\mathbf{u} \in \mathcal{H}^1(\Omega)} \max_{\boldsymbol{\lambda} \in \mathcal{H}^{-1/2}(\Gamma_u)} \left\{ \mathcal{E}_u(\mathbf{u}, d) - W_{\text{ext}} + \int_{\Gamma_u} \boldsymbol{\lambda} \cdot (\mathbf{u} - \hat{\mathbf{u}}) \, d\Gamma \right\} \quad (19)$$

Lagrange multipliers $\boldsymbol{\lambda}$ introduce an additional unknown at the boundary Γ_u , which can be interpreted as a traction, i.e. $\boldsymbol{\lambda} = \boldsymbol{\sigma}(\mathbf{u}) \cdot \mathbf{n}$ on Γ_u .

We discretise the Lagrange multipliers $\boldsymbol{\lambda}$ and the displacement field \mathbf{u} on Γ_u using Powell-Sabin B-splines:

$$\boldsymbol{\lambda} = \sum_{k=1}^{N_{bv}} \sum_{j=1}^3 N_k^j \boldsymbol{\lambda}_k^j = \mathbf{N}_b^e \boldsymbol{\lambda}_b^e, \quad \mathbf{u} = \sum_{k=1}^{N_{bv}} \sum_{j=1}^3 N_k^j \mathbf{U}_k^j = \mathbf{N}_b^e \mathbf{U}_b^e, \quad (20)$$

with N_{bv} the total number of vertices on the Dirichlet boundary Γ_u . The element shape function matrix \mathbf{N}_b^e has been given by Equation (11). $\boldsymbol{\lambda}_b^e$ and \mathbf{U}_b^e denote the degrees of freedom associated with the element boundaries. With this discretisation the 'displacement' sub-problem (19) yields the following system of equations:

$$\begin{bmatrix} \mathbf{K} & \mathbf{G} \\ \mathbf{G}^T & \mathbf{0} \end{bmatrix} \begin{bmatrix} \mathbf{u}^e \\ \boldsymbol{\lambda}^e \end{bmatrix} = \begin{bmatrix} \mathbf{F} \\ \mathbf{F}_L \end{bmatrix}, \quad (21)$$

where

$$\mathbf{K} = \int_{\Omega_e} \mathbf{B}^T \mathbf{D}(d) \mathbf{B} \, d\Omega \quad \mathbf{G} = \int_{\Gamma_u^e} \mathbf{N}^T \mathbf{N}_b \, d\Gamma \quad \mathbf{F} = \int_{\Gamma_t^e} \mathbf{N}^T \hat{\mathbf{t}} \, d\Gamma \quad \mathbf{F}_L = \int_{\Gamma_u^e} \mathbf{N}_b^T \hat{\mathbf{u}} \, d\Gamma, \quad (22)$$

and \mathbf{N} , \mathbf{N}_b the shape functions related to the element (Equation (10)) and the element boundary (Equation (11)), respectively. $\mathbf{D}(d)$ is the phase-field based element stiffness matrix, which relates the stress $\boldsymbol{\sigma}(\mathbf{u}, d)$ to the strain $\boldsymbol{\varepsilon}(\mathbf{u})$. In Voigt notation:

$$\boldsymbol{\sigma} = [\sigma_x, \sigma_y, \tau_{xy}]^T = \frac{\partial \mathcal{W}(\mathbf{u}, d)}{\partial \boldsymbol{\varepsilon}(\mathbf{u})} = \mathbf{D}(d) \boldsymbol{\varepsilon}(\mathbf{u}) = \mathbf{D}(d) \mathbf{B} \mathbf{u}^e \quad \text{and} \quad \boldsymbol{\varepsilon}(\mathbf{u}) = [\varepsilon_x, \varepsilon_y, \gamma_{xy}]^T \quad (23)$$

with $\mathbf{B} = \mathcal{L}(\mathbf{N})$ the strain-nodal displacement matrix where

$$\mathcal{L} = \begin{bmatrix} \partial/\partial x & 0 \\ 0 & \partial/\partial y \\ \partial/\partial y & \partial/\partial x \end{bmatrix} \quad (24)$$

As is well-known, the dimension of the system of equations (21) increases when adopting the Lagrange multiplier method. Moreover, the resulting stiffness matrix is no longer banded, nor positive definite.

3.3. Penalty method

By introducing a penalty parameter β , the 'displacement' sub-problem (3) can be modified as:

$$\mathbf{u} = \text{Arg} \min_{\mathbf{u} \in \mathcal{H}^1(\Omega)} \left\{ \mathcal{E}_u(\mathbf{u}, d) - W_{\text{ext}} + \frac{\beta}{2} \int_{\Gamma_u} (\mathbf{u} - \hat{\mathbf{u}})^2 \, d\Gamma \right\}, \quad (25)$$

which yields the following system of equations:

$$(\mathbf{K} + \mathbf{K}_p) \mathbf{u}^e = \mathbf{F} + \mathbf{F}_p \quad (26)$$

with

$$\mathbf{K}_p = \beta \int_{\Gamma_u^e} \mathbf{N}^T \mathbf{N} \, d\Gamma \quad \mathbf{F}_p = \beta \int_{\Gamma_u^e} \mathbf{N}^T \hat{\mathbf{u}} \, d\Gamma \quad (27)$$

Clearly, the dimension of the system of equation is now not increased. Moreover, the resulting matrix is symmetric and positive definite, provided that \mathbf{K} is symmetric and β is sufficiently large.

However, when increasing β , the system matrix will become ill-conditioned. A convergence rate of the order $h^{(2p+1)/3}$ in the energy norm can be achieved when [19]:

$$\beta = \eta h^{-(2p+1)/3}, \quad (28)$$

h being the element size and p being the order of the basis function order (here: $p = 2$). The constant η should be large enough to enforce the required boundary condition.

3.4. Nitsche's method

Nitsche's form for the 'displacement' sub-problem (3) can be stated as:

$$\mathbf{u} = \text{Arg} \min_{\mathbf{u} \in \mathcal{H}^1(\Omega)} \left\{ \mathcal{E}_u(\mathbf{u}, d) - W_{\text{ext}} - \int_{\Gamma_u} \boldsymbol{\sigma}(\mathbf{u}, d) \cdot \mathbf{n} \cdot (\mathbf{u} - \hat{\mathbf{u}}) \, d\Gamma + \frac{\beta}{2} \int_{\Gamma_u} (\mathbf{u} - \hat{\mathbf{u}})^2 \, d\Gamma \right\}, \quad (29)$$

yielding

$$[\mathbf{K} + \mathbf{K}_p - (\mathbf{K}_N + \mathbf{K}_N^T)] \mathbf{u}^e = \mathbf{F} + \mathbf{F}_p - \mathbf{F}_N \quad (30)$$

with

$$\mathbf{K}_N = \int_{\Gamma_u^e} \mathbf{B}^T \mathbf{D}(d) \hat{\mathbf{n}}^T \mathbf{N} \, d\Gamma \quad \mathbf{F}_N = \int_{\Gamma_u^e} \mathbf{B}^T \mathbf{D}(d) \hat{\mathbf{n}}^T \hat{\mathbf{u}} \, d\Gamma \quad (31)$$

where

$$\hat{\mathbf{n}} = \begin{bmatrix} n_{x_1} & 0 & n_{x_2} \\ 0 & n_{x_2} & n_{x_1} \end{bmatrix} \quad (32)$$

$\mathbf{n} = [n_{x_1}, n_{x_2}]$ being the normal vector of Dirichlet boundary Γ_u .

Like in the penalty method the dimension of the system of equations remains the same as that of \mathbf{K} . Also, the system of equations remains symmetric and positive definite, provided that \mathbf{K} is symmetric and β is large enough. However, the system equations may become ill-conditioned for increasing values of β . An optimal convergence in the \mathcal{L}^2 and energy norms can be attained if β is proportional to h^{-1} , i.e. $\beta = \eta h^{-1}$ [20].

3.5. Hellinger-Reissner (HR) principle

The H-R principle is introduced by two separate unknown fields, i.e., the displacement field \mathbf{u} and the stress field $\boldsymbol{\sigma}$, respectively. The energy functional related to the displacement sub-problem (3) is given as

$$\begin{aligned} \mathcal{E}_{H-R}(\mathbf{u}, \boldsymbol{\sigma}, d) &= \mathcal{E}^*(\mathbf{u}, \boldsymbol{\sigma}, d) - W_{\text{ext}} + \mathcal{E}_{h-r}(\mathbf{u}, \boldsymbol{\sigma}) \\ &= \int_{\Omega} \mathcal{W}(\mathbf{u}, \boldsymbol{\sigma}, d) \, d\Omega - \int_{\Gamma_t} \mathbf{u} \cdot \hat{\mathbf{t}} \, d\Gamma - \int_{\Gamma_u} \boldsymbol{\sigma} \cdot \mathbf{n} \cdot (\mathbf{u} - \hat{\mathbf{u}}) \, d\Gamma, \end{aligned} \quad (33)$$

and

$$(\mathbf{u}, \boldsymbol{\sigma}) = \text{Arg} \min_{\mathbf{u} \in \mathcal{H}^1(\Omega)} \max_{\boldsymbol{\sigma} \in \mathcal{L}^2(\Gamma_u)} \mathcal{E}_{H-R}(\mathbf{u}, \boldsymbol{\sigma}, d) \quad (34)$$

The stress field is also discretised using Powell-Sabin B-splines:

$$\boldsymbol{\sigma} = \sum_{k=1}^{N_v} \sum_{j=1}^3 N_k^j \boldsymbol{\sigma}_k^j = \mathbf{N}_s^e \boldsymbol{\sigma}^e, \quad (35)$$

linking to the strain via $\boldsymbol{\varepsilon}(\mathbf{u}) = \mathbf{D}(d)^{-1} \boldsymbol{\sigma}$.

From Equation (33) the resulting system of equations becomes:

$$\begin{bmatrix} \mathbf{0} & \mathbf{A}_s \\ \mathbf{A}_s^T & -\mathbf{K}_s \end{bmatrix} \begin{bmatrix} \mathbf{u}^e \\ \boldsymbol{\sigma}^e \end{bmatrix} = \begin{bmatrix} \mathbf{F} \\ -\mathbf{F}_s \end{bmatrix}, \quad (36)$$

with

$$\begin{aligned} \mathbf{K}_s &= \int_{\Omega_e} \mathbf{N}_s^T \mathbf{D}(d)^{-1} \mathbf{N}_s \, d\Omega & \mathbf{F}_s &= \int_{\Gamma_u^e} \mathbf{N}_s^T \hat{\mathbf{n}}^T \hat{\mathbf{u}} \, d\Gamma \\ \mathbf{A}_s &= \int_{\Omega_e} \mathbf{B}^T \mathbf{N}_s \, d\Omega - \mathbf{G}_s & \mathbf{G}_s &= \int_{\Gamma_u^e} \mathbf{N}^T \hat{\mathbf{n}} \mathbf{N}_s \, d\Gamma \end{aligned} \quad (37)$$

which leads to the following set of equations for the displacement:

$$\mathbf{A}_s^T \mathbf{u}^e = \mathbf{K}_s \mathbf{A}_s^{-1} \mathbf{F} - \mathbf{F}_s \quad (38)$$

Obviously, no additional variables have been added in the assembled set of equations for \mathbf{u}^e . However, due to the inverse of element stiffness matrix $\mathbf{D}(d)$ in \mathbf{K}_s , Equation (38) may lead to unstable solution when the solid is nearly broken due to $\mathbf{D}(d)|_{d \approx 1} \approx \mathbf{0}$. We will show unstable results in Section 4.2.

3.6. Linked Lagrange multiplier (LLM) method

The LLM method uses an additional stress field acting as Lagrange multipliers to impose the Dirichlet boundary condition [21]. Its original form modifies the weak form of 'displacement' sub-problem (3) directly: Find $\mathbf{u} \in \mathcal{H}^1(\Omega)$ and $\boldsymbol{\sigma} \in \mathcal{L}^2(\Gamma_u)$ such that

$$\begin{aligned} \int_{\Omega} \boldsymbol{\varepsilon}(\delta \mathbf{u}) : \boldsymbol{\sigma}(\mathbf{u}, d) \, d\Omega - \int_{\Omega} \delta \boldsymbol{\sigma} : (\boldsymbol{\varepsilon}(\boldsymbol{\sigma}) - \boldsymbol{\varepsilon}(\mathbf{u})) \, d\Omega - \int_{\Gamma_t} \mathbf{u} \cdot \hat{\mathbf{t}} \, d\Gamma \\ - \int_{\Gamma_u} \delta \mathbf{u} \cdot \boldsymbol{\sigma} \cdot \mathbf{n} \, d\Gamma - \int_{\Gamma_u} \delta \boldsymbol{\sigma} \cdot \mathbf{n} \cdot (\mathbf{u} - \hat{\mathbf{u}}) \, d\Gamma = 0, \end{aligned} \quad (39)$$

with $\boldsymbol{\sigma}(\mathbf{u}, d) = \mathbf{D}(d)\boldsymbol{\varepsilon}(\mathbf{u})$; $\boldsymbol{\varepsilon}(\boldsymbol{\sigma})$ is a function of the independent variable $\boldsymbol{\sigma}$, $\boldsymbol{\varepsilon}(\boldsymbol{\sigma}) = \mathbf{D}(d)^{-1}\boldsymbol{\sigma}$. Employing the discretisation for the stress in Equation (35), the weak form (39) leads to:

$$\begin{bmatrix} \mathbf{K} & -\mathbf{G}_s \\ \mathbf{A}_s^T & -\mathbf{K}_s \end{bmatrix} \begin{bmatrix} \mathbf{u}^e \\ \boldsymbol{\sigma}^e \end{bmatrix} = \begin{bmatrix} \mathbf{F} \\ -\mathbf{F}_s \end{bmatrix}, \quad (40)$$

yielding:

$$(\mathbf{K} + \mathbf{G}_s \mathbf{K}_s^{-1} \mathbf{A}_s^T) \mathbf{u}^e = \mathbf{F} + \mathbf{G}_s \mathbf{K}_s^{-1} \mathbf{F}_s \quad (41)$$

The LLM approach resembles the H-R principle and the Lagrange multiplier method. The classical Lagrange multiplier approach only addresses the variable difference (displacement) on the Dirichlet boundary. The LLM approach enforces the variable difference (strain) in the whole domain, see the second integral in Equation (39). Different from the H-R principle, the strain energy in the first integral in Equation (39) is given as a function of the displacement. More importantly, the inverse of \mathbf{K}_s in Equation (41) fixes the issue in the Hellinger-Reissner principle when the solid is nearly broken. Stable solutions are obtained in Section 4.2.

The LLM approach produces a non-symmetric system matrix (40). A modified version of the LLM approach has been proposed in [22]. The independent variable $\boldsymbol{\sigma}$ is only defined in the domain $\Omega_{\Gamma_u} \cup \Omega_{\Gamma_u}$ is the set of discretised triangle elements with at least one node or one side touching Dirichlet boundary Γ_u . The weak form in Equation (39) becomes:

$$\begin{aligned} \int_{\Omega} \boldsymbol{\varepsilon}(\delta \mathbf{u}) : \boldsymbol{\sigma}(\mathbf{u}, d) \, d\Omega - \frac{1}{m} \left[\int_{\Omega_{\Gamma_u}} \delta \boldsymbol{\sigma} : (\boldsymbol{\varepsilon}(\boldsymbol{\sigma}) - \boldsymbol{\varepsilon}(\mathbf{u})) \, d\Omega - \int_{\Omega_{\Gamma_u}} \boldsymbol{\varepsilon}(\delta \mathbf{u}) : (\boldsymbol{\sigma} - \boldsymbol{\sigma}(\mathbf{u})) \, d\Omega \right] \\ - \int_{\Gamma_t} \mathbf{u} \cdot \hat{\mathbf{t}} \, d\Gamma - \int_{\Gamma_u} \delta \mathbf{u} \cdot \boldsymbol{\sigma} \cdot \mathbf{n} \, d\Gamma - \int_{\Gamma_u} \delta \boldsymbol{\sigma} \cdot \mathbf{n} \cdot (\mathbf{u} - \hat{\mathbf{u}}) \, d\Gamma = 0, \end{aligned} \quad (42)$$

yielding

$$\begin{bmatrix} \mathbf{K} - \mathbf{K}_{\Gamma_u} & \mathbf{A}_{s2} \\ \mathbf{A}_{s2}^T & -\mathbf{K}_{s2} \end{bmatrix} \begin{bmatrix} \mathbf{u}^e \\ \boldsymbol{\sigma}^e \end{bmatrix} = \begin{bmatrix} \mathbf{F} \\ -\mathbf{F}_s \end{bmatrix}, \quad (43)$$

which leads to the assembled system equation for the displacement:

$$(\mathbf{K} - \mathbf{K}_{\Gamma_u} + \mathbf{A}_{s2} \mathbf{K}_{s2}^{-1} \mathbf{A}_{s2}^T) \mathbf{u}^e = \mathbf{F} - \mathbf{A}_{s2} \mathbf{K}_{s2}^{-1} \mathbf{F}_s \quad (44)$$

where

$$\begin{aligned} \mathbf{K}_{\Gamma_u} &= \frac{1}{m} \int_{\Omega_{\Gamma_u}^e} \mathbf{B}^T \mathbf{D}(d) \mathbf{B} \, d\Omega & \mathbf{K}_{s2} &= \frac{1}{m} \int_{\Omega_{\Gamma_u}^e} \mathbf{N}_s^T \mathbf{D}(d)^{-1} \mathbf{N}_s \, d\Omega \\ \mathbf{A}_{s2} &= \frac{1}{m} \int_{\Omega_{\Gamma_u}^e} \mathbf{B}^T \mathbf{N}_s \, d\Omega - \mathbf{G}_s, \end{aligned} \quad (45)$$

Clearly, the system equation (43) is symmetric and banded provided that \mathbf{K} is symmetric and banded. The modified LLM approach has been proven to be stable if $m > 1$ [23]. In addition, due to the inverse of \mathbf{K}_{s2} in Equation (43), unstable solutions are avoided, see Section 4.2.

4. NUMERICAL EXAMPLES

To assess the accuracy of the methodologies provided in previous sections, we will present two benchmark examples: a linear elastic problem with a known analytical solution, and a crack propagation problem with kinked crack paths.

Provided that no damage evolves in the solid, $d = 0$, Equation (2) becomes the energy functional for linear elastic problems. For the linear elastic problem given in Section 4.1, analytical solutions are available in the literature [24]. The performance of the approaches presented in Section 3 is assessed using the H^1 error norm. The error of each element is computed as [25]:

$$\|\mathbf{u} - \bar{\mathbf{u}}\|_{H^1(\Omega_e)} = \sqrt{\left(\int_{\Omega_e} (\mathbf{u} - \bar{\mathbf{u}})^T \cdot (\mathbf{u} - \bar{\mathbf{u}}) \, d\Omega + \int_{\Omega_e} (\mathbf{u} - \bar{\mathbf{u}})' \cdot (\mathbf{u} - \bar{\mathbf{u}})' \, d\Omega \right)} \quad (46)$$

where \mathbf{u} stands for the analytical solution, $\bar{\mathbf{u}}$ denotes the approximate solution, and $(\mathbf{u} - \bar{\mathbf{u}})'$ is the derivative of $(\mathbf{u} - \bar{\mathbf{u}})$ with respect to x_1 and x_2 , respectively. The domain error is obtained by summing up the element error:

$$\|\mathbf{u} - \bar{\mathbf{u}}\|_{H^1(\Omega)} = \sqrt{\sum_e \left(\|\mathbf{u} - \bar{\mathbf{u}}\|_{H^1(\Omega_e)} \right)^2} \quad (47)$$

The second example is dealing with kinked crack paths in a square plate. The energy functional in Equation (2) should be used fully with a strongly anisotropic surface energy model [8, 26]:

$$\mathcal{E}(\mathbf{u}, d) = \int_{\Omega} a(d) \mathcal{W}(\mathbf{u}) \, d\Omega - \int_{\Gamma_t} \mathbf{u} \cdot \hat{\mathbf{t}} \, d\Gamma + \frac{G_0}{\varpi \ell} \int_{\Omega} (w(d) + \ell^4 \nabla^2 d : \mathbf{C} : \nabla^2 d) \, d\Omega, \quad (48)$$

where ℓ is a regularization length, governing the width of the distributed crack. $a(d) = (1 - d)^2$ is a degradation function, $w(d) = 9d$ is a monotonically increasing function which represents the energy dissipation per unit volume, and $\varpi = 4 \int_0^1 \sqrt{w(d)} \, dd = 96/5$ is a normalisation parameter. $\nabla^2 d$ is a Hessian, i.e. $(\nabla^2 d)_{ij} = \frac{\partial^2 d}{\partial x_i \partial x_j}$ and \mathbf{C} is a positive-definite fourth-order tensor with the same symmetries as the linear elastic stiffness tensor [27]. Assuming a cubic symmetry, three material constants, C_{1111} , C_{1122} and C_{1212} , suffice to define \mathbf{C} . The damage evolution then follows from (in a strong format) [26, 28]:

$$\frac{2\ell^4 G_0}{\varpi} \left(2(C_{1122} + 2C_{1212}) \frac{\partial^4 d}{\partial x_1^2 \partial x_2^2} + C_{1111} \left(\frac{\partial^4 d}{\partial x_1^4} + \frac{\partial^4 d}{\partial x_2^4} \right) \right) + \mathcal{W}(\mathbf{u}) a'(d) \ell + \frac{G_0}{\varpi} w'(d) = 0, \quad (49)$$

complemented by the irreversibility condition $\dot{d} \geq 0$. The resulting anisotropic surface energy $G_c(\theta)$ then takes the form [26, 28]:

$$G_c(\theta) = G_0 \sqrt[4]{C(\theta)}, \quad (50)$$

with

$$C(\theta) = \frac{1}{4} (3C_{1111} + C_{1122} + 2C_{1212}) \left(1 + \frac{C_{1111} - C_{1122} - 2C_{1212}}{3C_{1111} + C_{1122} + 2C_{1212}} \cos \theta \right). \quad (51)$$

For crack propagation problem, two sub-problems in Equations (3) and (4) are solved iteratively. The 'displacement' sub-problem is constrained by Dirichlet boundary conditions. Section 3 addresses different approaches to enforce it. To assess the performance of these approaches, we will compare the crack propagation direction and the load-displacement response.

For the crack propagation direction, Chambolle has suggested that the underlying crack path selection is related to the generalised maximum energy release rate criterion (GMERR) [29]. The GMERR criterion postulates that the crack will propagate along the direction θ such that $G(\theta)/G_c(\theta)$ attains a maximum among all $\theta \in [-\pi, \pi]$. We will consider the prediction of the GMERR criterion as a reference solution for the crack propagation direction.

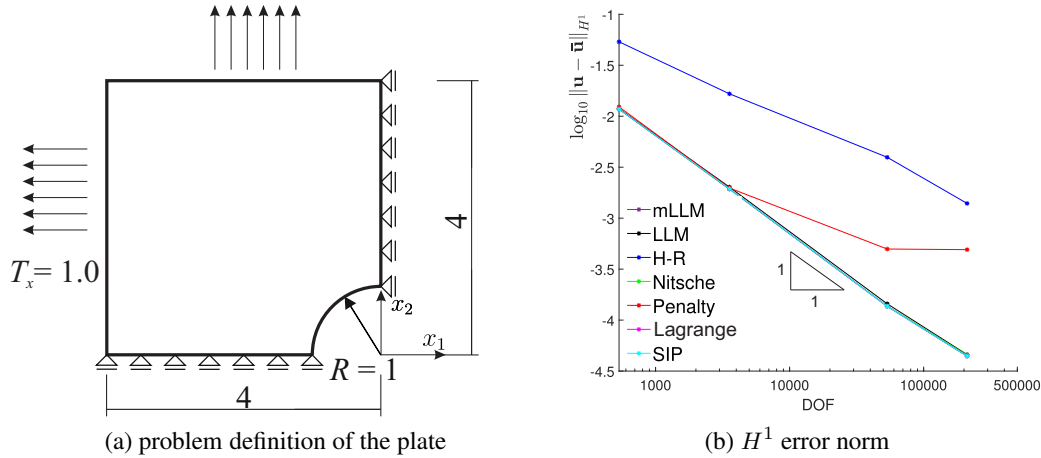


Figure 4. Linear elasticity: infinite plate with a circular hole – problem definition and H^1 error norm. For the penalty method and Nitsche's method, the penalty parameter is $\beta = 10^5$. In the figure, mLLM denotes the modified version of LLM method with the parameter $m = 10$ [22], while SIP represents the approach of strongly imposing Dirichlet boundary conditions.

4.1. Linear elasticity: infinite plate with a circular hole

We consider an infinite plate with a circular hole (radius $R = 1$ m), see Figure 4(a). For this problem, Speleers et al. [30] employed a quarter of an annulus to represent the infinite plate problem. Here we consider a square plate with a hole to address this problem. The material parameters are: Young's modulus $E = 100$ N/m², Poisson's ratio $\nu = 0.0$, and the thickness $h = 1$ m. The exact solutions for the radial and the tangential displacement are [31]:

$$\begin{aligned} u_r &= \frac{T_x r \cos(2\theta)}{2E} \left[(1 + \nu) + 4 \frac{R^2}{r^2} - (1 + \nu) \frac{R^4}{r^4} \right] + \frac{T_x r}{2E} \left[(1 - \nu) + (1 + \nu) \frac{R^2}{r^2} \right] \\ u_\theta &= -\frac{T_x r \sin(2\theta)}{2E} \left[(1 + \nu) + 2(1 - \nu) \frac{R^2}{r^2} + (1 + \nu) \frac{R^4}{r^4} \right] \end{aligned} \quad (52)$$

where θ is the azimuthal coordinate. From this, the stress components can be derived as:

$$\begin{aligned} \sigma_r &= \frac{T_x}{2} \left(1 - \frac{R^2}{r^2} \right) + \frac{T_x \cos 2\theta}{2} \left(\frac{3R^4}{r^4} - \frac{4R^2}{r^2} + 1 \right) \\ \sigma_\theta &= \frac{T_x}{2} \left(1 + \frac{R^2}{r^2} \right) - \frac{T_x \cos 2\theta}{2} \left(\frac{3R^4}{r^4} + 1 \right) \\ \sigma_{r\theta} &= \frac{T_x \sin 2\theta}{2} \left(\frac{3R^4}{r^4} - \frac{2R^2}{r^2} - 1 \right) \end{aligned} \quad (53)$$

The solution for this problem has a stress concentration at $(x_1, x_2) = (0, 1)$, but no singularity. Hence, an optimal rate of convergence $k = -p/2 = -2/2 = -1$ in the H^1 norm should be attained, see Figure 4(b). In the figure, most solutions approach the optimal solution where Dirichlet boundary conditions are imposed in a strong sense. Due to the influence of the penalty parameter β , the results of the penalty method diverge from the optimal convergence rate. The solution which derives from the H-R principle approaches the optimal rate of convergence, but the solution is not optimal because of the appearance of the inverse of \mathbf{D} in Equation (37).

Figures 5 and 6 show the solution in increasing values of the penalty parameter β for the penalty method and Nitsche's method, respectively. Figures 5(a) and 6(a) present convergence curves of different choice of β . The penalty method and Nitsche's method converge with a rate close to 1 in the H^1 error norm if the penalty parameter β is increasing. Due to the consistent term in Equation (29), Nitsche's method converges fast to the optimal solution when increasing β compared to the penalty method. Figures 5(b) and 6(b) show the condition number of the stiffness matrix for the penalty method and for Nitsche's method when increasing β . The condition number grows linearly with the penalty parameter. Obviously, the condition number becomes larger for denser discretisations, rendering the matrix ill-conditioned. The ill-conditioning reduces the applicability of the penalty method. For Nitsche's method, one can choose a small penalty parameter β to reduce the ill-conditioning at the expense of a reduced accuracy, see Figures 6(a) and 6(b). Figures 7 and 8 show the error of the maximum principle stress σ_1 for the penalty method and for Nitsche's method, respectively. The figures show a significant error level around the hole, where local refinement is essential to smoothen the stress gradient [6, 25].

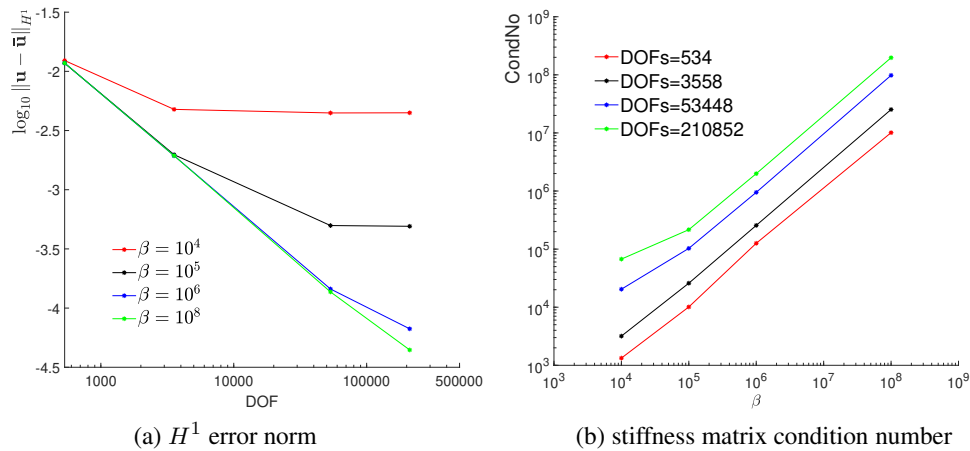


Figure 5. H^1 error norm for the penalty method and the condition number of the stiffness matrix.

4.2. Crack kinking in a square plate

We now consider a unit square domain with an initial crack under pure mode-I loading. Figure 9(a) shows the geometry and the boundary conditions. We consider the displacement at the boundary corresponding to the singular stress field (parameterised by the stress intensity factor K_I) around the initial crack tip. The asymptotic displacement fields are given by:

$$\begin{aligned} u_{x_1} &= \frac{K_I}{2\mu} \sqrt{\frac{r}{2\pi}} \cos \frac{\theta}{2} (\kappa - \cos \theta) \\ u_{x_2} &= \frac{K_I}{2\mu} \sqrt{\frac{r}{2\pi}} \sin \frac{\theta}{2} (\kappa - \cos \theta) \end{aligned} \quad (54)$$

where $\mu = E/2(1 + \nu)$, $\kappa = 3 - 4\nu$ for plane strain and $\kappa = (3 - \nu)/(1 + \nu)$ for plane stress conditions, and (r, θ) are polar coordinates with origin positioned at the crack tip. With a suitable

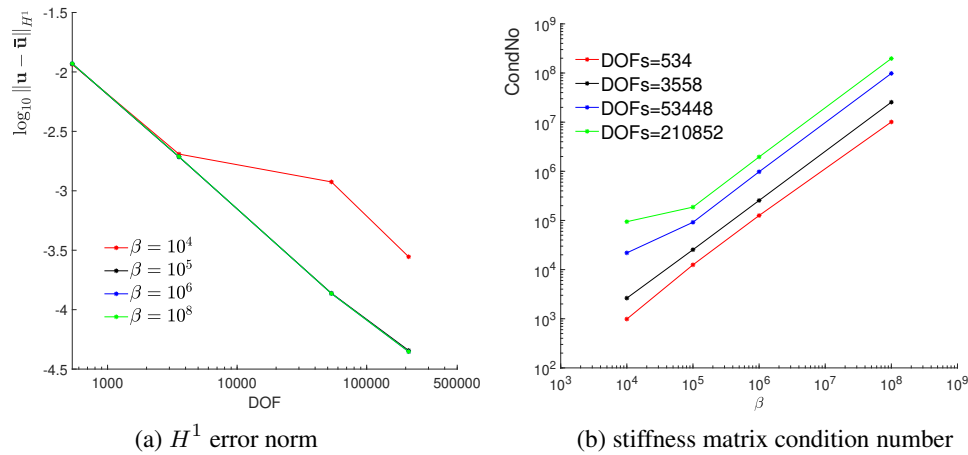


Figure 6. H^1 error norm for Nitsche's method and the condition number of the stiffness matrix.

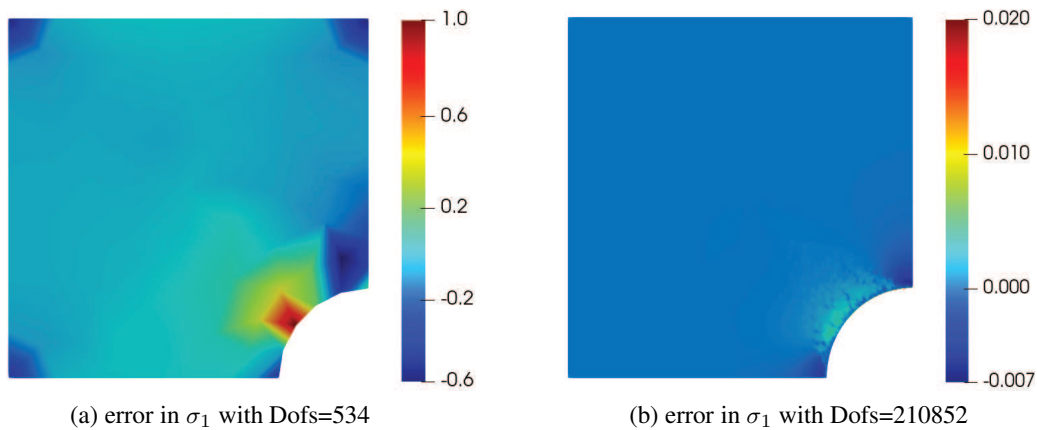


Figure 7. Error in maximum principal stress σ_1 for the penalty method (penalty parameter $\beta = 10^8$).

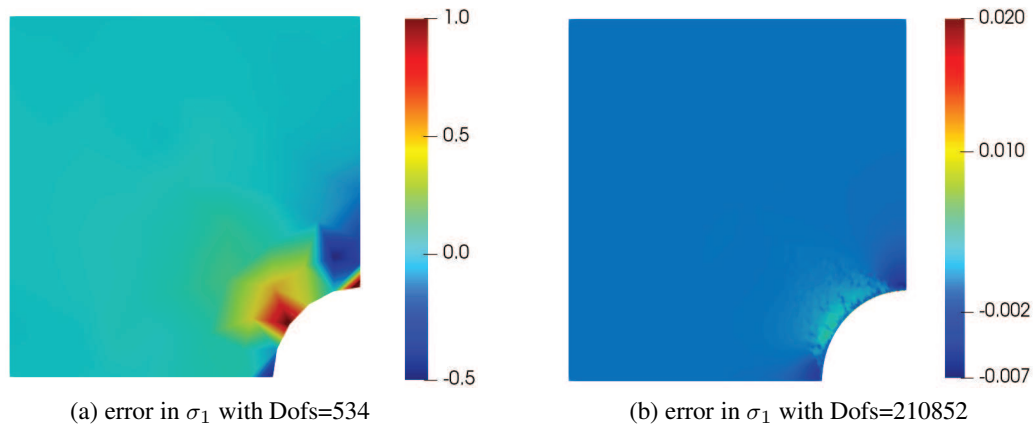


Figure 8. Error in maximum principal stress σ_1 for Nitsche's method (penalty parameter $\beta = 10^8$).

rescaling of the loading [32], we set the Young modulus $E = 1$. Poisson's ratio is set to $\nu = 0.3$. Plane-stress conditions are assumed.

Here, we consider the scaling surface energy $G_0 = 1$ and the strongly anisotropic surface energy of the form $G_c(\theta) = \sqrt[4]{1 + 0.8 \cos 4(\theta + \theta_0)}$ by setting the parameters $C_{1111} = 1.8$, $C_{1122} = -1.7$

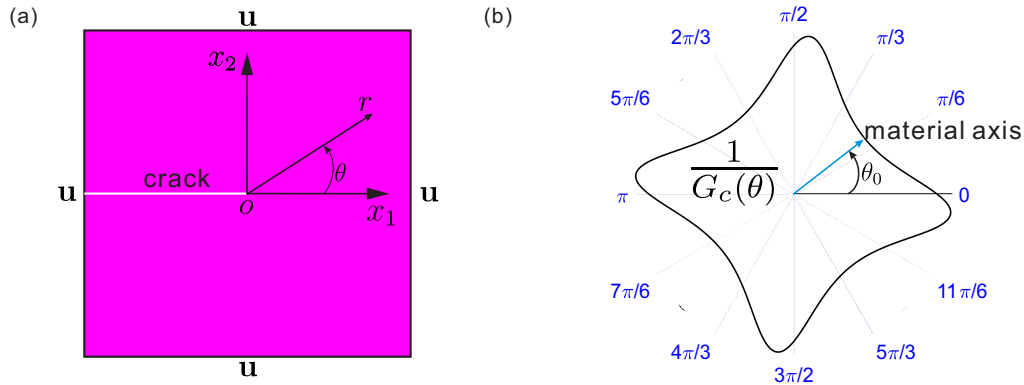


Figure 9. (a) Geometry and boundary conditions for a square plate. The displacement is applied at the boundary corresponding to the asymptotic crack field with a given mode-I (K_I) stress intensity factor. The initial crack is represented as two overlapping sides; (b) polar plot of the reciprocal surface energy $1/G_c(\theta)$, with $G_c(\theta) = \sqrt[4]{1 + 0.8 \cos 4(\theta + \theta_0)}$.

and $C_{1212} = 0.15$ in Eq. (50), and then apply the standard transformation for the rotation of \mathbf{C} over an angle θ_0 [33]. θ_0 denotes the material orientation with respect the x_1 -axis, see Figure 9(b). $\theta_0 = \pi/90$ has been chosen. The regularisation length is given as $\ell = 0.02$.

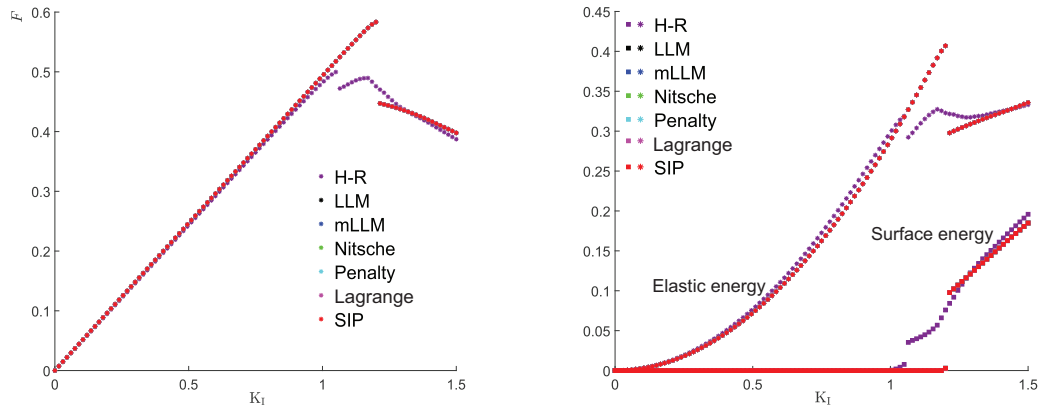


Figure 10. Load-displacement response and evolution of the elastic and surface energies. The force is obtained by summation of the loads in the x_2 -direction along the top boundary. The displacement is parameterised by the stress intensity factor K_I , see Equation (54). For the penalty method and Nitsche's method, the penalty parameter is $\beta = 10^8$. mLLM denotes the modified version of LLM method with the parameter $m = 10$ [22].

The computed load-displacement curve, as well as the elastic and surface energies are shown in Figure 10. In general, a good agreement is obtained between different approaches, except for the solution which derives from the H-R principle. Due to the inverse of $\mathbf{D}(d)$ in Equation (38), unstable solutions are obtained when the solid is nearly broken, yielding $\mathbf{D}(d)|_{d \approx 1} \approx \mathbf{0}$.

In Figure 10, the jump in the force and the energies relates to the re-initiation of the crack associated with an add-crack of a finite length appearing in a single time step [33], see Figure 11. The jump of the crack is consistent with theoretical analyses [29], which states that a kinking crack must be associated with a jump in time and space of the crack propagation.

Figure 11 shows the crack kinking path obtained from the phase-field model. The figure also presents the crack kinking angle θ derived from the GMERR criterion [33], indicated as the red arrow. Obviously, the results of the phase-field simulations well match that of the GMERR criterion, except for the solution which derives from the H-R principle because of the existence of the inverse of $\mathbf{D}(d)$. In general, the algorithm of imposing Dirichlet boundary condition well captures the crack

kinking behaviour, and well resolves the crack path, again with exception of the solution which derives from the H-R principle.

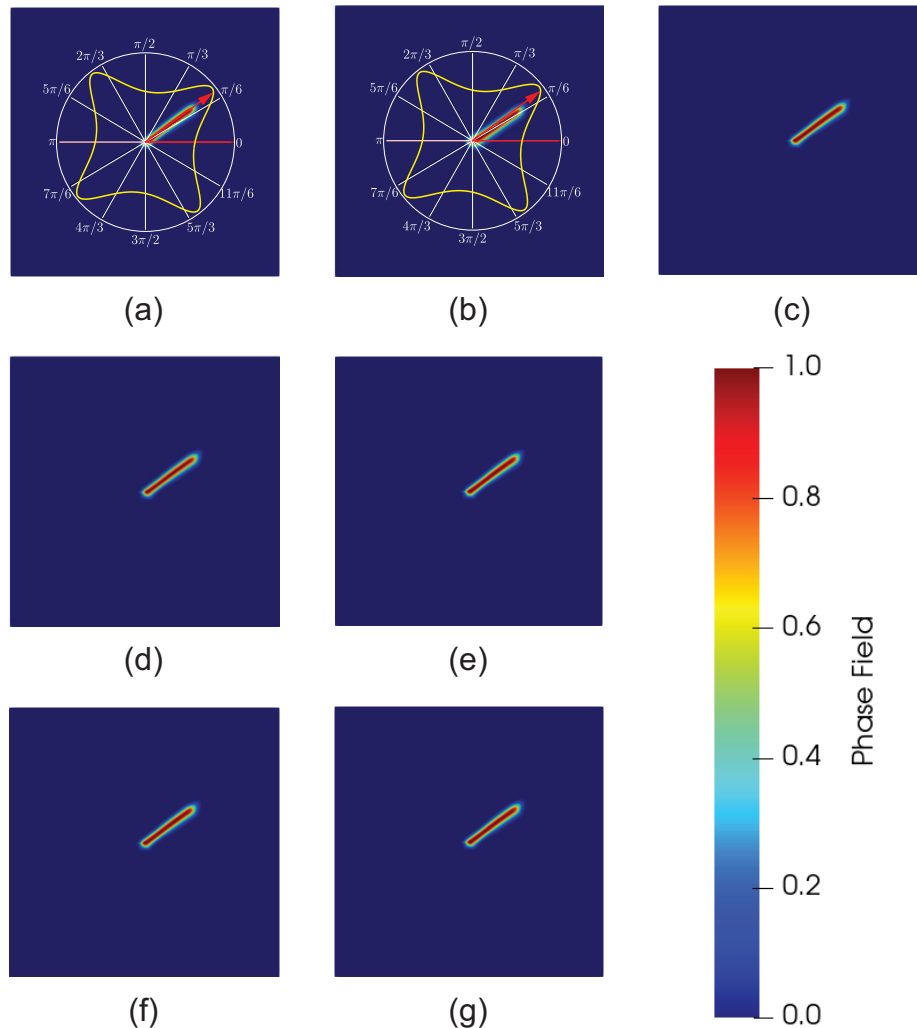


Figure 11. Contour plot of phase field d under $\theta_0 = \pi/90$: (a) strongly imposing Dirichlet boundary condition, (b) H-R principle method, (c) modified version of LLM method, (d) LLM method, (e) Nitsche's method, (f) penalty method, (g) Lagrange method. For the penalty method and Nitsche's method, the penalty parameter is $\beta = 10^5$. In the figure, the crack kinking angle θ from the GMERR criterion [33] is shown, indicated as the red arrow. The crack kinking angle θ only presents in figures (a) and (b) for conciseness.

5. CONCLUDING REMARKS

Weak approaches allow Dirichlet boundary conditions to be imposed in Powell-Sabin B-spline based analysis. In the current study, we have considered fracture problems using the phase field method. We have discussed imposing Dirichlet boundaries in a strong sense, the Lagrange multiplier and penalty methods, Nitsches method, the Hellinger-Reissner principle, the LLM method and its modified version. We have compared them in two case studies to assess the versatility and accuracy of these approaches.

For elastic problems, all approaches attain an optimal convergence rate. The penalty method and Nitsche's method require a special choice of the penalty parameter. The applicability of the penalty method is reduced due to the ill-conditioning of the resulting matrix and the lack of consistency of

the weak formulation. Nitsche's method introduces new terms in the weak form in order to maintain consistency and coercivity of the bilinear form. The H-R principle does not give an optimal solution due to the existence of the inverse of the stiffness matrix D . For fracture problems, most methods well capture the crack propagation, agree well with the GMERR criterion, with exception of the method which stems from the H-R principle because of the appearance of the inverse term $D(d)$.

ACKNOWLEDGEMENT

Financial support from the European Research Council (ERC Advanced Grant 664734 PoroFrac) is gratefully acknowledged.

DATA AVAILABILITY STATEMENT

Data sharing is not applicable to this article as no datasets were generated or analysed during this study.

CONFLICT OF INTEREST

The authors declare that there is no conflict of interest regarding the publication of this paper.

REFERENCES

- [1] Powell MJD, Sabin MA. Piecewise quadratic approximations on triangles. *ACM Transactions on Mathematical Software (TOMS)* 1977; **3**:316–325.
- [2] Speleers H, Manni C, Pelosi F, Sampoli ML. Isogeometric analysis with Powell-Sabin splines for advection-diffusion-reaction problems. *Computer Methods in Applied Mechanics and Engineering* 2012; **221**:132–148.
- [3] Giorgiani G, Guillard H, Nkonga B, Serre E. A stabilized Powell-Sabin finite-element method for the 2D Euler equations in supersonic regime. *Computer Methods in Applied Mechanics and Engineering* 2018; **340**:216–235.
- [4] May S, Vignollet J, de Borst R. Powell-Sabin B-splines and unstructured standard T-splines for the solution of Kirchhoff-Love plate theory using Bézier extraction. *International Journal for Numerical Methods in Engineering* 2016; **107**:205–233.
- [5] May S, de Borst R, Vignollet J. Powell-Sabin B-splines for smeared and discrete approaches to fracture in quasi-brittle materials. *Computer Methods in Applied Mechanics and Engineering* 2016; **307**:193–214.
- [6] Chen L, de Borst R. Cohesive fracture analysis using Powell-Sabin B-splines. *International Journal for Numerical and Analytical Methods in Geomechanics* 2019; **43**:625–640.
- [7] Chen L, Li B, de Borst R. Energy conservation during remeshing in the analysis of dynamic fracture. *International Journal for Numerical Methods in Engineering* 2019; **120**:433–446.
- [8] Chen L, Li B, de Borst R. The use of Powell-Sabin B-splines in a higher-order phase-field model for crack kinking. *Computational Mechanics* 2021; **67**:127–137.
- [9] Chen L, de Borst R. Phase-field modelling of cohesive fracture. *European Journal of Mechanics-A/Solids* 2021; :104343.

- [10] Speleers H, Dierckx P, Vandewalle S. Numerical solution of partial differential equations with Powell-Sabin splines. *Journal of Computational and Applied Mathematics* 2006; **189**:643–659.
- [11] Speleers H, Dierckx P, Vandewalle S. Powell-Sabin splines with boundary conditions for polygonal and non-polygonal domains. *Journal of Computational and Applied Mathematics* 2007; **206**:55–72.
- [12] Beirão Da Veiga L, Hughes TJR, Kiendl J, Lovadina C, Niiranen J, Reali A, Speleers H. A locking-free model for Reissner-Mindlin plates: Analysis and isogeometric implementation via NURBS and triangular NURPS. *Mathematical Models and Methods in Applied Sciences* 2015; **25**:1519–1551.
- [13] Lu K, Augarde CE, Coombs WM, Hu Z. Weak impositions of Dirichlet boundary conditions in solid mechanics: a critique of current approaches and extension to partially prescribed boundaries. *Computer Methods in Applied Mechanics and Engineering* 2019; **348**:632–659.
- [14] Francfort GA, Marigo JJ. Revisiting brittle fracture as an energy minimization problem. *Journal of the Mechanics and Physics of Solids* 1998; **46**:1319–1342.
- [15] Miehe C, Hofacker M, Welschinger F. A phase field model for rate-independent crack propagation: Robust algorithmic implementation based on operator splits. *Computer Methods in Applied Mechanics and Engineering* 2010; **199**:2765–2778.
- [16] Dierckx P. On calculating normalized Powell-Sabin B-splines. *Computer Aided Geometric Design* 1997; **15**:61–78.
- [17] Geuzaine C, Remacle JF. Gmsh: A 3-D finite element mesh generator with built-in pre-and post-processing facilities. *International Journal for Numerical Methods in Engineering* 2009; **79**:1309–1331.
- [18] O'Rourke J, Aggarwal A, Maddila S, Baldwin M. An optimal algorithm for finding minimal enclosing triangles. *Journal of Algorithms* 1986; **7**:258–269.
- [19] Babuška I. The finite element method with penalty. *Mathematics of Computation* 1973; **27**:221–228.
- [20] Nitsche J. Über ein Variationsprinzip zur Lösung von Dirichlet-Problemen bei Verwendung von Teilräumen, die keinen Randbedingungen unterworfen sind. *Abhandlungen aus dem Mathematischen Seminar der Universität Hamburg*, vol. 36, Springer, 1971; 9–15.
- [21] Gerstenberger A, Wall WA. An embedded Dirichlet formulation for 3d continua. *International Journal for Numerical Methods in Engineering* 2010; **82**:537–563.
- [22] Baiges J, Codina R, Henke F, Shahmiri S, Wall WA. A symmetric method for weakly imposing dirichlet boundary conditions in embedded finite element meshes. *International Journal for Numerical Methods in Engineering* 2012; **90**:636–658.
- [23] Codina R, Baiges J. Weak imposition of essential boundary conditions in the finite element approximation of elliptic problems with non-matching meshes. *International Journal for Numerical Methods in Engineering* 2015; **104**:624–654.
- [24] Chen L, Dornisch W, Klinkel S. Hybrid collocation-Galerkin approach for the analysis of surface represented 3D-solids employing SB-FEM. *Computer Methods in Applied Mechanics and Engineering* 2015; **295**:268–289.
- [25] Chen L, de Borst R. Adaptive refinement of hierarchical T-splines. *Computer Methods in Applied Mechanics and Engineering* 2018; **337**:220–245.

- [26] Li B, Peco C, Millán D, Arias I, Arroyo M. Phase-field modeling and simulation of fracture in brittle materials with strongly anisotropic surface energy. *International Journal for Numerical Methods in Engineering* 2015; **102**:711–727.
- [27] Chen L. Three-dimensional Greens function for an anisotropic multi-layered half-space. *Computational Mechanics* 2015; **56**:795–814.
- [28] Chen L, Li B, de Borst R. Adaptive isogeometric analysis for phase-field modeling of anisotropic brittle fracture. *International Journal for Numerical Methods in Engineering* 2020; **121**:4630–4648.
- [29] Chambolle A, Francfort GA, Marigo JJ. When and how do cracks propagate? *Journal of the Mechanics and Physics of Solids* 2009; **57**:1614–1622.
- [30] Speleers H, Manni C, Pelosi F. From NURBS to NURPS geometries. *Computer Methods in Applied Mechanics and Engineering* 2013; **255**:238–254.
- [31] de Borst R, Chen L. The role of Bézier extraction in adaptive isogeometric analysis: Local refinement and hierarchical refinement. *International Journal for Numerical Methods in Engineering* 2018; **113**:999–1019.
- [32] Farrell P, Maurini C. Linear and nonlinear solvers for variational phase-field models of brittle fracture. *International Journal for Numerical Methods in Engineering* 2017; **109**:648–667.
- [33] Li B, Maurini C. Crack kinking in a variational phase-field model of brittle fracture with strongly anisotropic surface energy. *Journal of the Mechanics and Physics of Solids* 2019; **125**:502–522.